Non-Newtonian power-law gravity currents propagating in confining boundaries

Noname manuscript No.
(will be inserted by the editor)

Non-Newtonian power-law gravity currents propagating in confining boundaries

Sandro Longo, Vittorio Di Federico,
Luca Chiapponi

Received: date / Accepted: date

Abstract The propagation of viscous, thin gravity currents of non-Newtonian liquids in horizontal and inclined channels with semicircular and triangular cross-sections is investigated theoretically and experimentally. The liquid rheology is described by a power-law model with flow behaviour index n, and the volume released in the channel is taken to be proportional to t^{α}, where t is time and α is a non-negative constant. Some results are generalised to power-law cross-sections. These conditions are representative of environmental flows, such as lava or mud discharges, in a variety of conditions. Theoretical solutions are obtained in self-similar form for horizontal channels, and with the method of characteristics for inclined channels. The position of the current front is found to be a function of the current volume, the liquid rheology, and the channel inclination and geometry. The triangular cross-section is associated with the fastest or slowest propagation rate depending on whether $\alpha < \alpha_c$ or $\alpha > \alpha_c$. For horizontal channels, $\alpha_c = n/(n+1) < 1$, whereas for inclined channels, $\alpha_c = 1$, irrespective of the value of n. Experiments were conducted with Newtonian and power-law liquids by independently measuring the rheological parameters and releasing currents with constant volume ($\alpha = 0$) or constant volume flux ($\alpha = 1$) in right triangular and semicircular channels. The experimental results validate the model for horizontal channels and inclined channels with $\alpha = 0$. For tests in inclined

S. Longo
Dipartimento di Ingegneria Civile, Ambiente Territorio e Architettura (DICATeA), Università di Parma, Parco Area delle Scienze, 181/A, 43124 Parma, Italy
Tel.: +39 0521 905157
Fax: +39 0521 905924
E-mail: sandro.longo@unipr.it

V. Di Federico
Dipartimento di Ingegneria Civile, Chimica, Ambientale e dei Materiali (DICAM), Università di Bologna, Viale Risorgimento, 2, 40136 Bologna, Italy

L. Chiapponi
Dipartimento di Ingegneria Civile, Ambiente Territorio e Architettura (DICATeA), Università di Parma, Parco Area delle Scienze, 181/A, 43124 Parma, Italy

channels with $\alpha = 1$, the propagation rate of the current front tended to lower values than predicted, and different flow regimes were observed, i.e., uniform flow with normal depth or instabilities resembling roll waves at an early stage of development. The theoretical solution accurately describes current propagation with time before the transition to longer roll waves. An uncertainty analysis reveals that the rheological parameters are the main source of uncertainty in the experiments and that the model is most sensitive to their variation. This behaviour supports the use of carefully designed laboratory experiments as rheometric tests.

Keywords Gravity current · Similarity solution · Non-Newtonian · Power-law · Channel shape · Laboratory experiments

1 Introduction

Gravity currents occur in several natural phenomena (e.g., mud flows and lava flows) and manufacturing processes (e.g., coating processes and mould filling) and are characterised by a large variety of physical conditions and approximations, as discussed in the reviews of Simpson [1], Huppert [2], and Ungarish [3]. Models of gravity currents of Newtonian fluids, in which buoyancy and viscous or inertial forces are balanced, have been successfully tested in experiments by Huppert [4] and Didden and Maxworthy [5]. However, fluids exhibiting purely Newtonian behaviour are an exception to the rule that most fluids in the environment, in biology, and in industrial processes behave as non-Newtonian fluids. Experimental evidence from both field and laboratory studies demonstrates that some magmas behave as non-Newtonian fluids at subliquidus temperatures due to gas bubbles and the presence of crystals [6]. Numerous factors influence the propagation of magma flows, such as thermal effects that cause an increase in the apparent viscosity eventually inducing a crustal layer at the surface, accompanied by an increase in the flow resistance. However, the early stage of lava eruption is not affected by these factors and can be confidently modelled within the simplified framework of the present model [7]. Mudflows in surface and submarine settings also exhibit complex rheological behaviour when treated with a single phase approach; for a review, see Ugarelli and Di Federico [8]. Although the fluid rheology in these environmental flows is often best described by a yield stress model, the relatively simple Ostwald-de Waele power-law approximation is appropriate for describing the behaviour of fresh magma, fine sediment-water mixtures, and mine tailings in the limit that the yield stress tends to zero [9–11]. Gravity current models of power-law fluids have been developed by, among others, Pascal [12], Gratton et al. [13], and Di Federico et al. [14] and experimentally tested by Chowdhury and Testik [15], Sayag and Worster [16], and Longo et al. [17]. In some analyses, the estimation of fluid parameters relies on the measurement of the slumping of a constant volume of power-law fluid on a horizontal base [18]. The inference of non-Newtonian rheological parameters by experiments with gravity currents is extensively analysed in [17]. Jacobson and Testik [19] experimentally investigated the entrainment of ambient water into constant volume release gravity currents of power-law fluid. In many cases, the flow of gravity currents is confined by channels [20, 21], as in lava flows [7] and mud dynamics [22]. The shape of the boundaries influences the velocity of

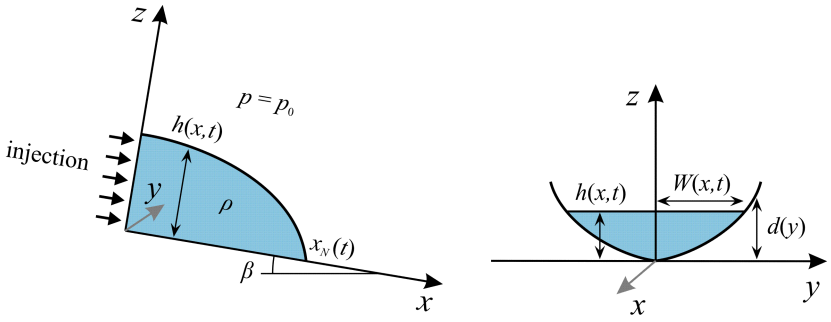

Fig. 1 A sketch of the current in the x-z and y- z planes.

the front and significantly modifies the overall dynamics of the current. The goals of the present study are to develop solutions for gravity currents of power-law liquids flowing in confined channels and to test them experimentally. In Section 2, governing equations are derived for the cases of flow in a horizontal channel and flow in an inclined rectilinear channel, caused by the release of a volume of liquid varying as t^α. Two subsections present self-similar solutions (horizontal case) and solutions using the method of characteristics (inclined case) for semicircular and triangular channels. A third subsection generalises some results to channels described by a power function. In Sections 3 and 4, theoretical results are compared with laboratory experiments conducted at constant volume or constant volume flux with shear-thinning, Newtonian, and shear-thickening (only in a single test) fluids in three different channels. Section 3 describes the experimental setting and procedures, and Section 4 discusses the experimental results and presents an uncertainty analysis. A set of conclusions in Section 5 closes the paper.

2 Formulation

Consider a non-Newtonian liquid with rheology parameterised by an Ostwald-de Waele power-law relating the shear stress and the shear rate $\tau = \widetilde{\mu}\dot{\gamma}|\dot{\gamma}|^{n-1}$, where τ is the shear stress, $\widetilde{\mu}$ the consistency index, n the fluid behaviour index, and $\dot{\gamma}$ the shear rate. A liquid of uniform density, ρ, is injected into a rectilinear channel of fixed cross-section inclined at an angle β with the horizontal, and moves in an ambient fluid of negligible mass density (due to the large density difference between the current and the ambient fluid). The channel geometry is shown in Figure 1, with the x, y, and z orthogonal axes oriented along the channel axis, across the channel, and normal to the slope, respectively. The cross-section of the channel, with a boundary described by the function $d(y)$, is partly occupied by the current, which has a top width of $2W(x,t)$ and a height $h(x,t)$ that is invariant in the span-wise direction. We assume that buoyancy and viscous forces are balanced with negligible inertial effects and that the motion is quasi-stationary and can be described by continuity and momentum balance with null acceleration. Assuming that the streamlines are parallel to the bottom of the channel and neglecting the effects of surface tension, the pressure

in the liquid is hydrostatic and given by

$$p = p_0 + \rho g(h-z)\cos\beta, \tag{1}$$

where p_0 is the atmospheric pressure at the free surface and g is the gravitational acceleration. We also assume that the extent of the flow, $x_N(t)$, is much larger than both h and W. Hence, the motion is taken to be unidimensional along the x-axis and is described by a single velocity component $u(x,y,z,t)$. Under these hypotheses, the Stokes equation reduces to

$$-\frac{\partial p}{\partial x} + \rho f_x + \frac{\partial \tau_{yx}}{\partial y} + \frac{\partial \tau_{zx}}{\partial z} = 0, \tag{2}$$

where ρf_x is the volume force in the x-direction and τ_{yx}, τ_{zx} are the shear stresses. We also consider wide cross-sections with $h << W$, allowing one to neglect $\partial\tau_{yx}/\partial y$ with respect to $\partial\tau_{zx}/\partial z$. Under this hypothesis, substitution of the expression for the shear stress of a power-law fluid into Eq.(2) yields

$$\frac{\partial}{\partial z}\left[\left(\frac{\partial u}{\partial z}\right)^n\right] = -S, \tag{3}$$

where the assumption $\partial u/\partial z > 0$ holds and the source term S, dependent on the channel inclination angle β, is given by

$$S = -\frac{\rho g}{\widetilde{\mu}}\frac{\partial h}{\partial x}\ (\beta = 0),\ \ S = \frac{\rho g}{\widetilde{\mu}}\sin\beta\ (\beta \neq 0). \tag{4}$$

Eq. (4) indicates that for a horizontal channel, the motion is induced by the slope of the free surface, while for an inclined channel, it is assumed that the current is locally in equilibrium, with gravity acting proportionally to the slope. The latter condition also requires that $\tan\beta >> \partial h/\partial x$ and excludes the possibility that the effect of the free-surface slope is comparable with that of the channel slope. The dynamic boundary condition at the free surface requires the continuity of the shear stress in the liquid and in the ambient fluid, which can be approximated by zero. The no-slip condition holds at the fixed boundary. Hence, Eq. (3) can be integrated by imposing

$$u|_{z=d} = 0,\ \ \left.\frac{\partial u}{\partial z}\right|_{z=h} = 0, \tag{5}$$

such that we obtain

$$u(x,y,z,t) = S^{1/n}\frac{n}{n+1}\left[(h-d)^{(n+1)/n} - (h-z)^{(n+1)/n}\right]. \tag{6}$$

The local continuity equation for a one-dimensional current is

$$\frac{\partial A}{\partial t} + \frac{\partial Q}{\partial x} = 0, \tag{7}$$

where A is the cross-sectional area occupied by the liquid, given in the symmetric case by

$$A(x,t) = 2\int_0^{W(x,t)} [h(x,t) - d(y)]\,\mathrm{d}y, \tag{8}$$

and Q is the downstream volume flux obtained by integrating the velocity over the cross-sectional area. Substituting Eq.(8) into Eq.(7) yields

$$2W\frac{\partial h}{\partial t}+\frac{\partial Q}{\partial x}=0. \tag{9}$$

The global continuity equation yields

$$\int_0^{x_N(t)} A\,\mathrm{d}x = qt^{\alpha}, \tag{10}$$

where $q>0$ and $\alpha\geq 0$ are constants and qt^{α} is the volume of liquid released. The case $\alpha=0$ corresponds to instantaneous injection of a constant volume and $\alpha=1$ corresponds to constant volume flux. At the front end of the current, the boundary condition of vanishing height

$$h\left[x_N(t),t\right]=0 \tag{11}$$

completes the mathematical statement of the problem for horizontal channels. However, Eq. (11) cannot be satisfied for inclined channels as the order of the differential equation is lower due to the assumptions made in Eq. (4). For the inclined case this produces a profile ending abruptly at the head of the current, as noted by Huppert [23].

2.1 Semicircular cross-section

For a semicircular cross-section of radius r, the boundary is given by $d=r-(r^2-y^2)^{1/2}$ and the current half-width by $W=(2rh)^{1/2}[1-(1/2)h/r]^{1/2}$. Assuming that the current is thin compared to the radius, i.e., $h<<r$, it follows that the approximations $d\approx y^2/(2r)$, $W\approx(2rh)^{1/2}$, and $A\approx 4/3(2rh^3)^{1/2}$ hold. The relative error in the approximation of the width is $O(h/r)$; for $h/r=0.1$ and $h/r=0.5$ the relative error is equal to 2.6% and 15.5%, respectively. By integrating Eq.(6), the volume flux is obtained as

$$Q(x,t)=2\int_0^{W(x,t)}\mathrm{d}y\int_{d(y)}^{h(x,t)} u\mathrm{d}z = h^{5/2+1/n}\sqrt{r}S^{1/n}K_c(n), \tag{12}$$

where

$$K_c(n)=\frac{\sqrt{2\pi}\,\Gamma\left(2+1/n\right)}{\Gamma\left(7/2+1/n\right)}, \tag{13}$$

where $K_c(n)$ is a numerical factor and $\Gamma(\cdot)$ is the gamma function. Substituting the expression for the cross-sectional area into Eq. (10) yields

$$\frac{4}{3}\sqrt{2r}\int_0^{x_N(t)} h^{3/2}\mathrm{d}x = qt^{\alpha}. \tag{14}$$

2.1.1 The case $\beta = 0$ for a semicircular cross-section

For a horizontal channel with inclination angle $\beta = 0$, Eq. (9) yields

$$h^{1/2}\frac{\partial h}{\partial t} - \frac{\sqrt{2}}{4}K_c\left(\frac{\rho g}{\widetilde{\mu}}\right)^{1/n}\frac{\partial}{\partial x}\left(h^{5/2+1/n}\left|\frac{\partial h}{\partial x}\right|^{1/n-1}\frac{\partial h}{\partial x}\right) = 0. \tag{15}$$

Introducing the length and time scales

$$x^* = \left(\frac{q}{\sqrt{r}}\right)^{2n/(2\alpha+5n)}\left(\frac{\widetilde{\mu}}{\rho g}\right)^{2\alpha/(2\alpha+5n)}, \tag{16}$$

$$t^* = \left(\frac{q}{\sqrt{r}}\right)^{-2/(2\alpha+5n)}\left(\frac{\widetilde{\mu}}{\rho g}\right)^{5/(2\alpha+5n)}, \tag{17}$$

Eqs. (15) and (14) become

$$H^{1/2}\frac{\partial H}{\partial T} - \frac{\sqrt{2}}{4}K_c\frac{\partial}{\partial X}\left(H^{5/2+1/n}\left|\frac{\partial H}{\partial X}\right|^{1/n-1}\frac{\partial H}{\partial X}\right) = 0, \tag{18}$$

$$\int_0^{X_N(T)} H^{3/2}\,\mathrm{d}X = \frac{3\sqrt{2}}{8}T^{\alpha}, \tag{19}$$

respectively, and the boundary condition (11) is given by

$$H\left[X_N(T), T\right] = 0, \tag{20}$$

where $H = h/x^*$, $X = x/x^*$ and $T = t/t^*$ are nondimensional variables. The similarity solution of Eqs. (18-19) is expressed in terms of the similarity variable

$$\eta = \left(\frac{2\sqrt{2}}{K_c}\right)^{n/(n+1)} XT^{-F_{1c}},\ F_{1c} = \frac{2\alpha(n+2)+3n}{5n+7} \tag{21}$$

and the solution form

$$H(X,T) = \eta_N^{(n+1)/(n+2)}T^{F_{2c}}\psi(\zeta),\quad \zeta = \frac{\eta}{\eta_N},\quad F_{2c} = \frac{F_{1c}(n+1)-n}{n+2}, \tag{22}$$

where η_N is the value of η at the current edge X_N, and the shape function, ψ, is the solution of the nonlinear ordinary differential equation

$$\left(\psi^{5/2+1/n}\left|\psi'\right|^{1/n-1}\psi'\right)' - F_{2c}\psi^{3/2} + F_{1c}\zeta\psi^{1/2}\psi' = 0,\ \psi(1) = 0, \tag{23}$$

in which the prime indicates $\mathrm{d}/\mathrm{d}\zeta$. The value of η_N is obtained from Eq. (19), which transforms into

$$\eta_N = \left[\frac{4\sqrt{2}}{3}\left(\frac{K_c\sqrt{2}}{4}\right)^{n/(n+1)}\int_0^1 \psi^{3/2}\mathrm{d}\zeta\right]^{-F_{3c}},\ F_{3c} = \frac{2(n+2)}{5n+7}. \tag{24}$$

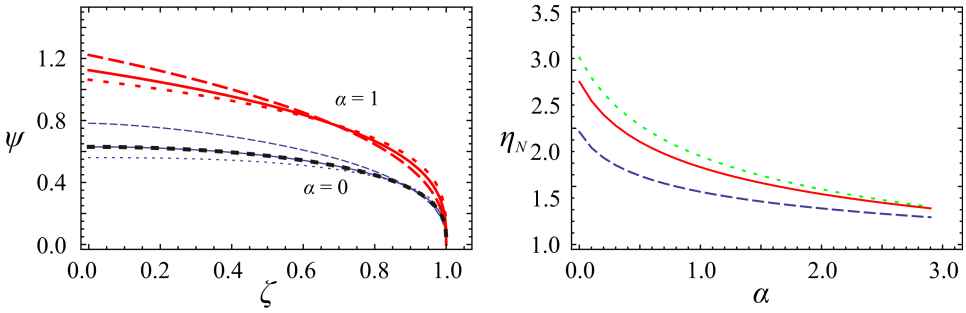

Fig. 2 Left panel: shape functions for semicircular horizontal channel sections for $n = 0.5$ (dashed line), $n = 1.0$ (solid line), and $n = 1.5$ (dotted line). The thick dotted line represents the analytical solution for $n = 1.0$. Right panel: the prefactor η_N as a function of α for $n = 0.5$ (dashed line), $n = 1.0$ (solid line), and $n = 1.5$ (dotted line). For $n = 1.0$ and $\alpha = 0$ the analytical solution $\eta_N = 2.9021$ is reproduced.

In Eqs. (21)-(24), the factors F_{1c}, F_{2c}, and F_{3c} take different values depending on the fluid rheology. For $\alpha = 0$, Eqs. (23) and (24) admit the following analytical solutions:

$$\psi = \left(\frac{n+2}{n+1}\right)^{1/(n+2)} \left(\frac{2F_{1c}}{3}\right)^{n/(n+2)} (1-\zeta^{n+1})^{1/(n+2)}, \tag{25}$$

$$\eta_N = \left(\frac{3\sqrt{2}}{8}\right)^{F_{3c}} \left(\frac{2\sqrt{2}}{K_c}\right)^{\frac{nF_{3c}}{n+1}} \left(\frac{n+1}{n+2}\right)^{\frac{3F_{3c}}{2(n+2)}} \left(\frac{3}{2F_{1c}}\right)^{\frac{3nF_{3c}}{2(n+2)}} \times \left[\frac{\Gamma\left[1+\frac{1}{1+n}+\frac{3}{2(2+n)}\right]}{\Gamma\left(1+\frac{1}{1+n}\right)\Gamma\left[1+\frac{3}{2(2+n)}\right]}\right]^{F_{3c}}, \tag{26}$$

which, for $n = 1$, are equivalent to the expressions given by Takagi and Huppert [20]. For $\alpha \neq 0$, Eq. (23) must be integrated numerically. To do so, a second boundary condition is obtained by generating an asymptotic solution near the current front in terms of a power series [4], to yield

$$\psi'(\zeta \to 1) = -a_0 b(1-\zeta)^{b-1},\ a_0 = \left(\frac{2F_{1c}}{3b^{1/n}}\right)^{nb},\ b = \frac{1}{n+2}. \tag{27}$$

Figure 2 shows the shape function for different values of α and n, and the prefactor η_N as a function of α for different values of n. The shape function significantly increases for increasing α and modestly decreases for increasing n, and the prefactor η_N increases for increasing n. The numerical result for $\alpha = 0$ is confirmed by the analytical solution. From Eq. (21), the front end of the current propagates as $X_N \propto T^{F_{1c}}$, with a speed $U_{X_N} \propto T^{F_{1c}-1}$.

2.1.2 The case $\beta > 0$ for a semicircular cross-section

For an inclined channel with $\beta > 0$, Eq. (9) becomes

$$\frac{\partial h}{\partial t} + \frac{K_c\sqrt{2}}{4}\left(\frac{\rho g}{\widetilde{\mu}}\right)^{1/n}\frac{(5n+2)}{2n}(\sin\beta)^{1/n}h^{1+1/n}\frac{\partial h}{\partial x} = 0, \tag{28}$$

where the factor K_c is given by Eq. (13). The dimensionless form of Eq. (28) is

$$\frac{\partial H}{\partial T} + \frac{K_c\sqrt{2}}{4}\frac{(5n+2)}{2n}(\sin\beta)^{1/n}H^{1+1/n}\frac{\partial H}{\partial X} = 0, \tag{29}$$

while Eq. (19) is unchanged. The function H is constant along the characteristics given by

$$\frac{\mathrm{d}X}{\mathrm{d}T} = g_c(n)H^{1+1/n},\ g_c(n) = \frac{K_c\sqrt{2}}{4}\frac{(5n+2)}{2n}(\sin\beta)^{1/n} \tag{30}$$

and admits the solution

$$H = g_c^{-n/(n+1)}X^{n/(n+1)}T^{-n/(n+1)}. \tag{31}$$

Eq. (31) represents a profile abruptly ending at X_N, which can be smoothed by including surface tension [23]. The condition $X_N = 0$ for $T = 0$, implicit in Eq. (31), can be changed to $X_N > 0$ for $T = 0$ by introducing a time shift equivalent to a virtual origin; this is a local effect without significant consequences for the current profile in the asymptotic regime. Note that no further boundary conditions are required. Upon substitution of Eq. (31), the constraint represented by Eq. (19) gives the length of the current as

$$X_N = \left(\frac{3\sqrt{2}}{8}\right)^{\frac{2(n+1)}{5n+2}} g_c^{\frac{3n}{5n+2}}\left[\frac{5n+2}{2(n+1)}\right]^{\frac{2(n+1)}{5n+2}} T^{\frac{2\alpha(n+1)+3n}{5n+2}} \tag{32}$$

with the front end advancing with a speed $U_{X_N} \propto T^{2(\alpha-1)(n+1)/(5n+2)}$. The current accelerates (decelerates) for $\alpha > 1$ ($\alpha < 1$). For $\alpha = 0$ and $n = 1$, the expressions given in dimensional form by Takagi and Huppert [20] are recovered.
For $\alpha = 1$, the volume flux, Q, is constant with $Q \equiv q$, the maximum height of the current at $X = X_N$ is equal to

$$H_{X_N} = \left[\frac{2(n+1)}{3n}K_c(\sin\beta)^{1/n}\right]^{-2n/(5n+2)}, \tag{33}$$

and the front end advances with a constant speed. The depth predicted by Eq. (33) may be compared with the normal and critical depths of the channel for the same volume flux. The normal depth is derived by balancing the gravitational force and tangential stress such that

$$h_n = \left[\frac{\widetilde{\mu}^{1/n}Q}{\sqrt{r}K_c(\rho g\sin\beta)^{1/n}}\right]^{2n/(5n+2)}, \tag{34}$$

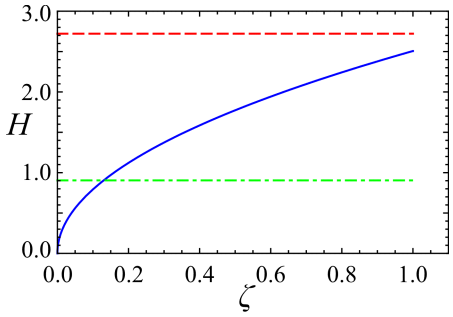

Fig. 3 The nondimensional profile of the gravity current in a semicircular inclined channel (bold line) with $\alpha = 1.0$, $n = 1.0$, and Fr $= 0.11$. The dashed line is the normal depth and the dash-dotted line is the critical depth.

yielding, in nondimensional form,

$$H_n = \left[K_c(\sin\beta)^{1/n}\right]^{-2n/(5n+2)}. \tag{35}$$

The critical depth, where energy is at a minimum for a given volume flux, is equal to

$$h_c = \left(\frac{27\chi Q^2}{64gr}\right)^{1/4}, \tag{36}$$

where χ is the Coriolis coefficient.

A comparison between the maximum depth at the current front calculated with the present model, as given by Eq. (33), and the normal depth yields $H_{X_N} > H_n$, $H_{X_N} = H_n$, or $H_{X_N} < H_n$, depending on whether $n > 2$, $n = 2$, or $n < 2$.

The global Reynolds and Froude numbers of the current are computed for inclined channels ($\beta > 0$) and constant volume flux ($\alpha = 1$) as

$$\mathrm{Re} = \frac{8\rho U_n^2}{\widetilde{\mu}}\left[\frac{\sqrt{2rh_n}}{2U_n}\right]^n, \quad \mathrm{Fr} = \frac{U_n}{\sqrt{\frac{2gh_n\cos\beta}{3\chi}}}, \tag{37}$$

where U_n is the normal velocity. Figure 3 shows the nondimensional profile of the current for $n = 1.0$ and Fr $= 0.11$. Similar results are obtained for other values of n (but are not shown here).

2.2 Triangular cross-section

The velocity distribution for laminar flow in a V-shaped cross-section with vertex angle 2θ cannot be computed by assuming $\partial\tau_{zx}/\partial z >> \partial\tau_{yx}/\partial y$ in the Stokes equation (2) for general values of θ, but only for $2\theta >> 90^\circ$. For Newtonian liquids, Takagi and Huppert [20] adopted a coordinate transformation and found a solution for

the velocity field in terms of an infinite summation of orthogonal cosine functions, deriving by integration an expression for the volume flux in the form

$$Q \approx \frac{0.137m^3}{1+m^2} h^4 S, \tag{38}$$

where $m = \tan\theta$ and S is the source term defined by Eq. (4). For a power-law liquid, a similar approach cannot be followed due to nonlinearity. Hence we resort to an empirical approach and employ the experimental results of Burger et al. [11]. They investigated the flow of various non-Newtonian liquids in open channels of different cross-sectional shapes and expressed the relationship between the Fanning friction factor, f, and the generalised Reynolds number, Re_H, in fully developed laminar flow through the use of a shape factor coefficient (the theoretical formulation given by Muzychka and Edge [24] yields similar results). For a power-law liquid flowing in a right triangular section with $2\theta = 90^\circ$, their experiments yielded

$$f = 14.6/\mathrm{Re}_H, \tag{39}$$

with

$$f = \frac{2gR\sin\beta}{U^2},\ \mathrm{Re}_H = \frac{8\rho U^2}{\widetilde{\mu}} \left(\frac{R}{2U}\right)^n, \tag{40}$$

where $U = Q/A$ and R is the hydraulic radius. Hence, by substituting the expressions given for f and Re_H in Eq. (40) into Eq. (39) we obtain

$$Q = K_t(n,m) h^{(3n+1)/n} S^{1/n},$$
$$K_t(n,m) = 2^{(3-2n)/n} \frac{m^{(2n+1)/n}}{(1+m^2)^{(n+1)/(2n)}} \left(\frac{1}{14.6}\right)^{1/n}, \tag{41}$$

where $K_t(n,m)$ is a coefficient incorporating the shape of the cross-section and the fluid rheology. For $n = 1$, K_t is approximately equal to the value 0.137 given in Eq. (38). Eq. (41) is thus strictly valid only for $2\theta = 90^\circ$. For other values of the vertex angle, 2θ, a factor solely dependent on channel shape and with a numerical value different from 14.6 will appear in the expression for the friction factor given by Eq. (39); this numerical factor must be determined with independent experiments similar to those of Burger et al. [11]. This will, in turn, change the numerical value of the coefficient $K_t(n,m)$ given by Eq. (41), but not its dependence on m and n. Hence. in the following theoretical derivations $K_t(n,m)$ is assumed to be known, regardless of its actual value.

2.2.1 The case $\beta = 0$ for a triangular cross-section

For a horizontal channel ($\beta = 0$), substituting Eq. (41) into Eq. (9) with $W = mh$ yields

$$h\frac{\partial h}{\partial t} - \frac{K_t}{2m}\left(\frac{\rho g}{\widetilde{\mu}}\right)^{1/n} \frac{\partial}{\partial x}\left(h^{(3n+1)/n}\left|\frac{\partial h}{\partial x}\right|^{1/n-1}\frac{\partial h}{\partial x}\right) = 0, \tag{42}$$

while Eq. (10) becomes

$$m\int_0^{x_N(t)} h^2 \mathrm{d}x = qt^{\alpha}, \tag{43}$$

because $A = mh^2$ and the boundary condition given by Eq. (11) holds. Introducing the length and time scales

$$x^* = \left(\frac{q}{m}\right)^{n/(\alpha+3n)} \left(\frac{\widetilde{\mu}}{\rho g}\right)^{\alpha/(\alpha+3n)}, \tag{44}$$

$$t^* = \left(\frac{q}{m}\right)^{-1/(\alpha+3n)} \left(\frac{\widetilde{\mu}}{\rho g}\right)^{3/(\alpha+3n)}, \tag{45}$$

Eqs. (42) and (43) become, in dimensionless form,

$$H\frac{\partial H}{\partial T} - \frac{K_t}{2m}\frac{\partial}{\partial X}\left(H^{(3n+1)/n}\left|\frac{\partial H}{\partial X}\right|^{1/n-1}\frac{\partial H}{\partial X}\right) = 0, \tag{46}$$

$$\int_0^{X_N(T)} H^2 \mathrm{d}X = T^{\alpha}, \tag{47}$$

and the boundary condition is again given by Eq. (20). The similarity variable and the solution form of the problem described by Eqs. (46)-(47), with Eq. (20), are given by

$$\eta = \left(\frac{2m}{K_t}\right)^{n/(n+1)} XT^{-F_{1t}},\ F_{1t} = \frac{\alpha(n+2)+2n}{3n+4}, \tag{48}$$

$$H(X,T) = \eta_N^{(n+1)/(n+2)} T^{F_{2t}} \psi(\zeta),\ \zeta = \frac{\eta}{\eta_N},\ F_{2t} = \frac{\alpha(n+1)+n}{3n+4}, \tag{49}$$

where the shape function, ψ, is obtained by solving the differential equation

$$\left(\psi^{(3n+1)/n}\left|\psi'\right|^{1/n-1}\psi'\right)' - F_{2t}\psi^2 + F_{1t}\zeta\psi\psi' = 0,\ \psi(1) = 0, \tag{50}$$

and the prefactor is given by

$$\eta_N = \left[\left(\frac{K_t}{2m}\right)^{n/(n+1)} \int_0^1 \psi^2 \mathrm{d}\zeta\right]^{-F_{3t}},\ F_{3t} = \frac{n+2}{3n+4}. \tag{51}$$

In Eqs. (48)-(51), the factors F_{1t}, F_{2t}, and F_{3t} depend solely on fluid rheology. For $\alpha = 0$, a closed form solution is derived as

$$\psi = \left(\frac{n}{3n+4}\right)^{n/(n+2)} \left(\frac{n+2}{n+1}\right)^{1/(n+2)} \left(1-\zeta^{n+1}\right)^{1/(n+2)}, \tag{52}$$

$$\eta_N = \left(\frac{2m}{K_t}\right)^{nF_{3t}/(n+1)} \left(\frac{3n+4}{n}\right)^{2nF_{3t}/(n+2)} \left(\frac{n+1}{n+2}\right)^{2F_{3t}/(n+2)} \times \left[{}_2F_1\left(\frac{1}{1+n}, -\frac{2}{2+n}, \frac{2+n}{1+n}, 1\right)\right]^{-F_{3t}}, \tag{53}$$

where ${}_2F_1$ is the hypergeometric function. For the case $n=1$, Eq. (53) is equivalent to the solution reported in dimensional form in [20]. For $\alpha \neq 0$, the numerical integration of Eq. (50) requires a second boundary condition near the current front, obtained similarly to Eq. (27) as

$$\psi'(\zeta \to 1) = -a_0 b(1-\zeta)^{b-1},\ a_0 = \left(\frac{nF_{1t} b^{(n-1)/n}}{b(3n+2)-1} \right)^{nb},\ b = \frac{1}{n+2}. \tag{54}$$

Numerical values of the shape function and the prefactor η_N for different values of α and n are similar to the semicircular case. The front end of the current propagates as $X_N \propto T^{F_{1t}}$ and advances with a speed $U_{X_N} \propto T^{F_{1t}-1}$.

2.2.2 *The case $\beta > 0$ for a triangular cross-section*

In an inclined triangular channel with $\beta > 0$, Eq. (9) becomes

$$\frac{\partial h}{\partial t} + \frac{K_t}{2m} \left(\frac{\rho g}{\widetilde{\mu}} \right)^{1/n} \frac{(3n+1)}{n} (\sin\beta)^{1/n} h^{(n+1)/n} \frac{\partial h}{\partial x} = 0, \tag{55}$$

and Eq. (43) is unchanged. In nondimensional form, Eq. (55) is

$$\frac{\partial H}{\partial T} + \frac{K_t}{2m} \frac{(3n+1)}{n} (\sin\beta)^{1/n} H^{(n+1)/n} \frac{\partial H}{\partial X} = 0, \tag{56}$$

while Eq. (20) still holds. The solution is obtained with the method of characteristics as

$$H = g_t^{-n/(n+1)} X^{n/(n+1)} T^{-n/(n+1)},\ g_t = \frac{K_t}{2m} \frac{(3n+1)}{n} (\sin\beta)^{1/n}, \tag{57}$$

and the length of the current is given by

$$X_N = \left(\frac{3n+1}{n+1} \right)^{(n+1)/(3n+1)} g_t^{2n/(3n+1)} T^{\frac{\alpha(n+1)+2n}{3n+1}}, \tag{58}$$

with the front end advancing with a speed $U_{X_N} \propto T^{(\alpha-1)(n+1)/(3n+1)}$. For $\alpha = 1$ (constant volume flux), the maximum height of the current at $X = X_N$ is equal to

$$H_{X_N} = \left(\frac{n+1}{2n} \frac{K_t}{m} \sin\beta^{1/n} \right)^{-n/(3n+1)}, \tag{59}$$

and the front end advances with constant speed. For $\alpha = 0$ and $n = 1$, the solution given by Takagi and Huppert [20] is recovered. The normal depth is given in dimensional and nondimensional form by

$$h_n = \left[\frac{\widetilde{\mu}^{1/n} Q}{K_t (\rho g \sin\beta)^{1/n}} \right]^{n/(3n+1)},\ H_n = \left[\frac{K_t}{m} (\sin\beta)^{1/n} \right]^{-n/(3n+1)}, \tag{60}$$

and the critical depth is

$$h_c = \left(\frac{2\chi Q^2}{g m^2} \right)^{1/5}. \tag{61}$$

The Reynolds and Froude numbers of the current are computed for constant volume flux ($\alpha = 1$) as

$$\mathrm{Re} = \frac{8\rho U_n^2}{\widetilde{\mu}}\left[\frac{mh_n}{4U_n(1+m^2)}\right]^n, \quad \mathrm{Fr} = \frac{U_n}{\sqrt{\frac{2gh_n\cos\beta}{2\chi}}}. \tag{62}$$

Hence, $H_{X_N} > H_n$, $H_{X_N} = H_n$, or $H_{X_N} < H_n$ depending on whether $n < 1$, $n = 1$, or $n > 1$.

2.3 A generalisation for power-law channels

The previous results can be suitably generalised upon describing the cross-section with a general power-law relationship $d = a\,|y/a|^k$, where a is a length scale and k is a prescribed constant: $k = 1$, $k = 2$, and $k \to \infty$ correspond to triangular, semicircular, and infinitely wide rectangular sections, respectively. For $k > 1$, the current depth is much smaller than its width and $\partial\tau_{zx}/\partial z >> \partial\tau_{yx}/\partial y$, as earlier hypothesised for semicircular sections. By using the same arguments for semicircular sections, for wide cross-sections ($k > 1$) the exponent of time, proportional to the propagation distance, c, is given by

$$c_{hw} = \frac{2k\alpha + n(1+k+k\alpha)}{1+n+k(3+2n)}, \qquad \text{for } \beta = 0, \tag{63}$$

$$c_{iw} = \frac{\alpha k(n+1)+n(k+1)}{n(k+1)+k(n+1)}, \qquad \text{for } \beta > 0. \tag{64}$$

In a narrow channel, the Stokes equation (2) simplifies, retaining only the gradient of the shear stress $\partial\tau_{yx}/\partial y$, which is the dominant term. By dimensional arguments, for propagation in narrow cross-sections ($k < 1$), the exponent of time is

$$c_{hn} = \frac{\alpha(k+1)+n(k+\alpha+1)}{2+2n+k(2+n)}, \qquad \text{for } \beta = 0, \tag{65}$$

$$c_{in} = \frac{\alpha+n(k+\alpha+1)}{1+n(2+k)}, \qquad \text{for } \beta > 0. \tag{66}$$

Note that $c_{iw}(\alpha,n,k) \equiv c_{in}(\alpha,n,1/k)$. A summary of the propagation rates for different geometries is listed in Table 1. In horizontal channels, the front end accelerates if $\alpha > (4+n)/(2+n)$ for V-shaped sections, $\alpha > (7+2n)/(4+2n)$ for semicircular sections, and $\alpha > (3+2n)/(2+n)$ for wide rectangular sections. For generic power-law cross-sections, accelerated currents are obtained for $\alpha > (2+2k+n)/(1+k+n)$, $k < 1$, and $\alpha > (1+3k+kn)/(2k+kn)$, $k > 1$. In inclined channels of any shape, the current front accelerates if $\alpha > 1$, decelerates if $\alpha < 1$, and advances with a constant speed independent of the value of the fluid behaviour index n if $\alpha = 1$. In horizontal channels, the front velocity attains its maximum value for a triangular section ($k = 1$) when $\alpha < \alpha_c \equiv n/(n+1)$; in this case the front is always decelerated. Conversely, if $\alpha > \alpha_c \equiv n/(n+1)$ the minimum value of the front velocity is reached for a triangular section; here the front can be decelerated or accelerated. Qualitatively

Shape	Reference	Horizontal ($\beta = 0$)	Reference	Inclined ($\beta > 0$)
Narrow ($k = 1/2$)	tp	$\frac{3(n+\alpha)+2n\alpha}{5n+6}$	tp	$\frac{2\alpha(n+1)+3n}{5n+2}$
V-shaped ($k = 1$)	tp	$\frac{\alpha(n+2)+2n}{3n+4}$	tp	$\frac{\alpha(n+1)+2n}{3n+1}$
Semicircular ($k = 2$)	tp	$\frac{2\alpha(n+2)+3n}{5n+7}$	tp	$\frac{2\alpha(n+1)+3n}{5n+2}$
Rectangular ($k \to \infty$)	GM	$\frac{\alpha(n+2)+n}{2n+3}$	tp	$\frac{\alpha(n+1)+n}{2n+1}$

Table 1 Current propagation rates in horizontal and inclined channels of different shapes. "GM" and "tp" refer to Gratton et al. [13] and this paper, respectively. For $n = 1$, these results are consistent with the data listed in Table I of Takagi and Huppert [21].

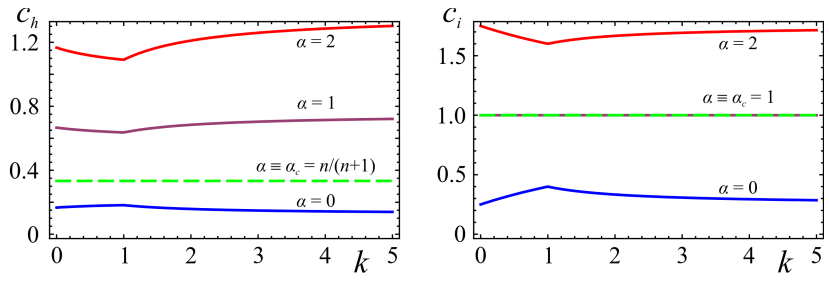

Fig. 4 The time exponent c (proportional to the propagation distance) as a function of k for a shear-thinning liquid with $n = 0.5$ for different values of α for horizontal (left panel) and inclined channels (right panel).

similar results are obtained for inclined channels, except that the critical value α_c equals unity, irrespective of the value of the flow behaviour index n. Figure 4 shows the dependence of the exponent of time, c, on k for a shear-thinning liquid ($n = 0.5$) for different values of α for horizontal and inclined channels, confirming the above findings. The influence of the shape of the cross-section, parameterised by k, is larger in the interval $0 < k < 2$. The results for different values of n (not shown here) are similar, indicating the relatively minor influence of the flow behaviour index n on the propagation rates. The values of α_c for $n = 1$ are in agreement with those reported in Takagi and Huppert [21].

3 Experiments

A series of experiments was performed at the Hydraulics Laboratory of the University of Parma to test the theoretical formulation. Constant volume ($\alpha = 0$) and constant volume flux ($\alpha = 1$) tests were conducted with Newtonian ($n = 1$), shear-thinning ($n < 1$), and shear-thickening ($n > 1$) liquids, in horizontal ($\beta = 0$) and inclined ($\beta > 0$) channels with different cross-sectional shapes. Three different experimental setups were utilised. The first employed a 600 mm-long circular tube of polymethyl methacrylate (PMMA) with a radius of 119 mm, which was cut along a

meridian plane and supported with frames and adjustable feet to ensure horizontality of the axis. This semicircular channel was used in experiments with $\alpha = 1$ and $\beta = 0$. Another set of experiments, conducted with $\alpha = 0$ and $\beta = 0$, and with $\alpha = 0$ or 1 and $\beta > 0$, used a circular 2000 mm-long PVC tube with a radius of 74.5 mm, which was fixed to an aluminium rigid frame supported by adjustable feet. In a third set of experiments, a 2000 mm-long aluminium profile with a triangular L-shaped 100 mm $\times$ 100 mm cross-section and a vertex angle of 90° was utilized, supported at both ends with plastic frames equipped with adjustable feet. To explain some apparent inconsistencies in the experimental results, the aluminium frame was covered with PVC in a limited subset of experiments (see the Discussion section). In all groups of tests, the inclination of the channel axis was measured with an electronic spirit level with an overall accuracy of 0.1°. For tests involving an instantaneous release of the liquid ($\alpha = 0$), a lock gate was installed at one end of the channel, delimiting a reservoir having the same cross-sectional shape. The volume of the liquid was estimated with a relative uncertainty of $\pm 1.5\%$ by weighing the mass that filled the reservoir and dividing by the mass density. For tests with a constant volume flux ($\alpha = 1$), a syringe pump built in the lab, accurate to $\pm 1\%$ of the instantaneous volume flux, delivered the liquid through a plastic tube. The position of the front end of the current was detected using either a high-resolution digital video camera or a digital camera with images taken approximately 600 mm above the current, thus achieving a spatial resolution of ≈ 3 pixels/mm. To cover the entire extent of the current with adequate spatial resolution, the video camera and one or two synchronised photo cameras were installed with overlapping fields of view, even though, for many tests, only the images far from the source were of interest. To identify the current boundary, the resulting images were processed using software that restituted the pixel positions in a reference grid with an overall estimated uncertainty of ± 1.5 mm. In the experiments with the lock gate, the start time was detected by observing the video images. In the other tests, the start of the syringe pump was controlled by a personal computer; simultaneously, an LED in the field of view of the video camera was turned on and an electric signal for acquiring an image was sent to the photo cameras. The video camera acquired 25 frames per second (usually undersampled to 1 frame per second or less) and the photo cameras acquired 1 frame per second or less, depending on the velocity of the front end of the current. The uncertainty in time measurement was assumed to be equal to 1/50 s for the video camera and negligible for the pictures taken by the photo cameras. The liquids used in the tests were prepared by gently mixing glycerol, water, and ink to obtain a Newtonian fluid, and by adding xanthan gum to obtain a shear-thinning fluid. The shear-thickening liquid used in a single test was a mixture of water (40% by weight) and cornstarch (60% by weight). The rheological behaviour of the liquids was tested with a coaxial cylinder shear rheometer (Haake Rotovisco RT10) and a parallel plate rheometer (Dynamic Shear Rheometer Anton Paar Physica MCR 101), both strain-controlled rheometers. The flow behaviour index and the consistency coefficient were obtained by fitting an Ostwald-de Waele power-law to the data measured with the rheometers. The real rheological behaviour of the liquid is generally better described by a Cross or Carreau-Yasuda model, which reduces to the power-law model only for limited ranges of the shear rate, with varying values of the indices in different ranges. Hence, to render the power-law approximation acceptable, the fit-

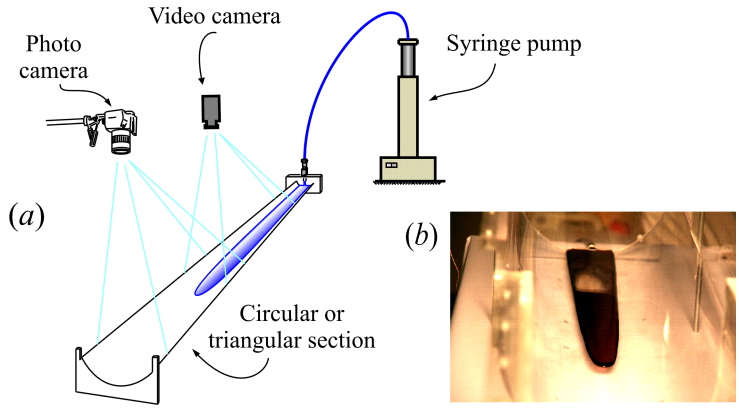

Fig. 5 (a) Schematic of the experimental apparatus. (b) A snapshot of a current propagating in a semicircular horizontal channel with constant volume flux. The image refers to Test 2.

ting was performed in the low shear rate range (less than 5 s^{-1}), consistent with the expected mean shear rate of the currents in the present experiments. The uncertainty associated with the rheological parameters is essentially due to the limitations of the power-law model in reproducing the rheometrical experimental data. For the liquids used in the present tests, the uncertainty (one standard deviation) associated with the flow behaviour index and the consistency coefficient are $\approx 2.5\%$ and $\approx 3.5\%$, respectively. The mass density of the liquids was measured by a hydrometer or by weighing a fixed known volume of liquid, with an uncertainty of $\approx 1\%$. The temperature was measured by submerging a mercury-in-glass thermometer (0.02 °C resolution) in the liquid before filling the syringe pump or the reservoir. Figure 5 shows a schematic of the experimental apparatus and a snapshot of a current of shear-thinning liquid advancing in a semicircular horizontal channel. A total of 36 tests were conducted with different channel cross-sections (semicircular and right triangular), inclinations to the horizontal, liquid supply methods (constant volume or volume flux), and rheologies. In most tests a shear-thinning fluid was used. Some tests employed a Newtonian fluid to validate the outcomes against known theoretical results. In a single test (test 55), a shear-thickening fluid was utilised. The experimental parameters are reported in Table 2, including: test number; channel inclination; type of test ($\alpha = 0$ or 1 for constant volume or volume flux); injected volume or volume flux; flow behaviour index and consistency coefficient; fluid density; and global Reynolds and Froude numbers for tests conducted with constant volume flux ($\alpha = 1$) in an inclined channel ($\beta > 0$).

We note that the highest observed value of the Reynolds number is $Re = 60$; this ensures that the Stokes flow approximation is correct, because the gradual transition from laminar to fully turbulent flow is expected to begin for $Re > 500$. In only two tests (25 and 42), the equivalent uniform flow in the channel is supercritical with a Froude number greater than unity (or, equivalently, with a normal depth less than the critical depth) and with the maximum height of the predicted profile smaller than the normal and critical depths. For the tests with $\mathrm{Fr} < 1$, the maximum height of the predicted profile is between the critical depth and the normal depth. A time shift

Test	shape	β (deg)	α	q (ml s$^{-\alpha}$)	n	$\widetilde{\mu}$ (Pa s^n)	ρ (kg m^{-3})	Re	Fr	state
21	c(2)	0.0	0.0	143.6	0.42	0.67	1175			
24	c(2)	0.0	0.0	311.2	0.42	0.67	1175			
52	c(2)	7.4	0.0	126	0.42	0.67	1175			
53	c(2)	4.5	0.0	130	0.42	0.67	1175			
55	c(2)	4.5	0.0	192	1.57	0.40	1200			
1	c(1)	0.0	1.0	1.35	0.42	0.67	1175			
2	c(1)	0.0	1.0	4.08	0.42	0.67	1175			
3	c(1)	0.0	1.0	0.57	0.42	0.67	1175			
5	c(1)	0.0	1.0	2.17	1.00	0.16	1241			
18	c(2)	4.0	1.0	0.79	1.00	0.16	1241	6.4	0.11	me
19	c(2)	4.0	1.0	0.78	0.42	0.67	1175	1.2	0.10	me
20	c(2)	5.5	1.0	2.34	0.42	0.67	1175	6.0	0.27	me
25	c(2)	30.6	1.0	3.94	0.42	0.67	1175	62.5	1.98	rw
26	c(2)	30.6	1.0	0.77	0.42	0.67	1175	9.8	0.76	rw
27	c(2)	30.6	1.0	0.21	0.42	0.67	1175	2.2	0.35	
28	c(2)	30.6	1.0	0.30	0.42	0.67	1175	3.3	0.43	rw
29	c(2)	30.6	1.0	0.24	0.42	0.67	1175	2.6	0.37	irw
30	c(2)	30.6	1.0	0.18	0.42	0.67	1175	1.9	0.32	
33	c(2)	18.0	1.0	0.94	0.42	0.67	1175	7.2	0.50	rw
34	c(2)	18.0	1.0	0.54	0.42	0.67	1175	3.9	0.36	
35	c(2)	18.0	1.0	1.64	0.42	0.67	1175	13.6	0.69	rw
9	t	0.0	0.0	286	0.42	0.67	1175			
10	t	0.0	0.0	430	0.42	0.67	1175			
14	t	5.5	0.0	163.9	0.42	0.67	1175			
15	t	8.8	0.0	68.0	0.42	0.67	1175			
16	t	5.5	0.0	104.1	0.42	0.67	1175			
6	t	0.0	1.0	2.14	0.42	0.67	1175			
7	t	0.0	1.0	0.54	0.42	0.67	1175			
8	t	0.0	1.0	4.33	0.42	0.67	1175			
11	t	5.5	1.0	4.14	0.42	0.67	1175	10.5	0.54	u
12	t	8.6	1.0	1.86	0.42	0.67	1175	7.6	0.57	u
13	t	5.5	1.0	0.81	0.42	0.67	1175	1.8	0.22	u
42	t	18.1	1.0	3.82	0.42	0.67	1175	40	1.93	
48	t	30.5	1.0	2.29	1.00	0.16	1241	3.3	0.78	me
49	t	30.5	1.0	3.62	1.00	0.16	1241	4.6	0.92	me
50	t	30.5	1.0	2.31	1.00	0.16	1241	3.3	0.78	u

Table 2 Experimental parameters for all tests. The symbols c(1) and c(2) indicate a semicircular section with $r = 119$ mm and $r = 74.5$ mm, respectively, whereas t indicates a triangular section with $2\theta = 90^\circ$. Values of global Reynolds and Froude numbers are listed when $\alpha = 1$ and $\beta > 0$. In the last column, "me" indicates a metastable state, "rw" indicates the presence of roll waves, "irw" indicates incipient roll waves, and "u" indicates uniform flow with normal velocity.

equivalent to a virtual origin was introduced to interpret the experimental data for the inclined channel and the constant volume subcase ($\alpha = 0$) for the horizontal channel. In the latter case, the correction was needed to account for the finite size of the reservoir and the finite time needed to open the gate.

4 Discussion

The scaled, nondimensional results for current front position as a function of time are depicted in Figure 6 for horizontal channels with semicircular cross-sections, and in Figure 7 for horizontal channels with right triangular cross-sections. Figures 8 and Figure 9 show the corresponding results for inclined channels. Each Figure is split into two panels (a) and (b), each covering a different range of abscissa and ordinate values. The different factors used for the scaling of X_N in the four Figures are expressed as $f_i(X_N)$, $i = 1,2,3,4$. Figures 8 and Figure 9, valid for inclined channels, depict two additional reference lines representing the normal speed of uniform currents of shear-thinning ($n = 0.42$) and Newtonian liquids. The inset in panel (a) of each Figure represents an enlargement of a portion of the panel.

For horizontal channels, the experimental results (symbols) are in good agreement with the theoretical predictions (solid lines) for constant volume flux ($\alpha = 1$) and constant volume ($\alpha = 0$). In the latter case, only the late time evolution of the current is consistent with the theory, while at early times the time exponent for the front end position differs from the similarity solution. This is because the current, after the slumping phase, is initially in an inertial-buoyancy regime, where buoyancy forces are balanced by inertia. The transition to a viscous-buoyancy regime takes longer for constant volume ($\alpha = 0$) than for constant volume flux ($\alpha = 1$) currents, as also noted by Sayag and Worster [16] for an axisymmetric geometry. For inclined channels, good agreement with the theory at late times was again observed in tests with $\alpha = 0$. In tests with $\alpha = 1$, the speed of the front was generally lower than the theoretical prediction, and different flow regimes were observed. In some tests conducted in triangular channels with small inclinations (up to 8.6°), the flow was stable, but the front of the current advanced with a constant speed lower than U_{X_N} predicted by Eq. (58) and equal to the mean velocity U_n in a channel with normal depth. The latter is significantly lower than the former, as shown by their ratio, which is given for semicircular and triangular channels by

$$\frac{U_{X_N}}{U_n} = (2+5n)\,[2(n+1)]^{-2(n+1)/(2+5n)}\,(3n)^{-3n/(2+5n)} \tag{67}$$

$$\frac{U_{X_N}}{U_n} = (1+3n)(n+1)^{-(n+1)/(1+3n)}(2n)^{-2n/(1+3n)}, \tag{68}$$

respectively. For both cross-sections, the numerical value of the ratio is always larger than unity, reaching a maximum of 2 for $n = 1$ and $n = 2$. For tests with larger channel inclinations (18.0° to 30.6°), streamwise instabilities developed with bores followed by gentle profiles. This phenomenon, known as roll waves, has been studied in the laminar regime by Julien and Hartley [25] for Newtonian fluids, Ng and Mei [10] for power-law shear-thinning fluids, and Longo [26] for power-law shear-thickening fluids. Roll waves start to form on uniform currents with a minimum length corresponding to the level of dissipation of the (uniform) flow and continue to grow with increasing lengths and bore speeds. Developed periodic roll waves in the flow of power-law shear-thinning liquids in rectangular channels show a peak fluid velocity exceeding the uniform current speed by$\approx$ 30% [10]. Although the dynamics of roll

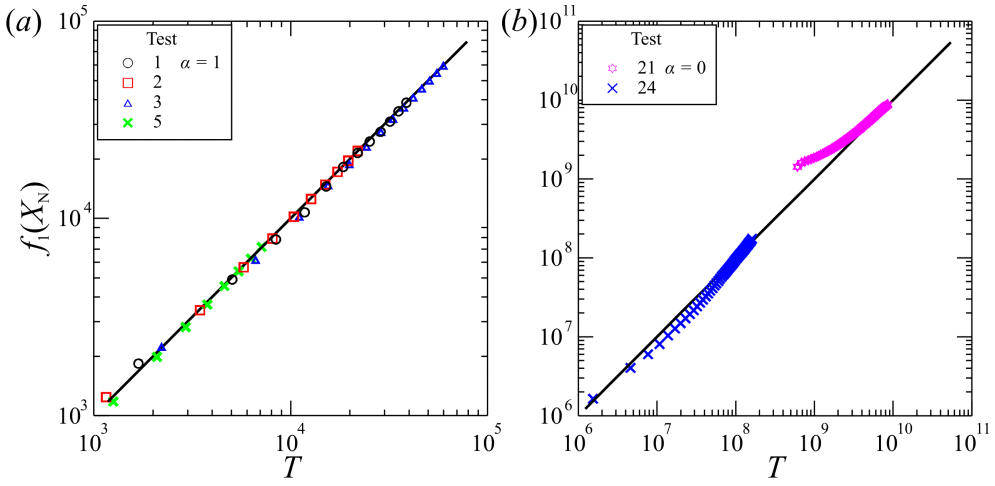

Fig. 6 Experimental results for horizontal semicircular channels in different sets of tests. The variables X_N and T are nondimensional and are scaled according to Eq. (21), with $f_1(X_N) = [(X_N/\eta_N)(2\sqrt{2}/K_c)^{n/(n+1)}]^{1/F_{1c}}$. The solid line represents the theoretical prediction.

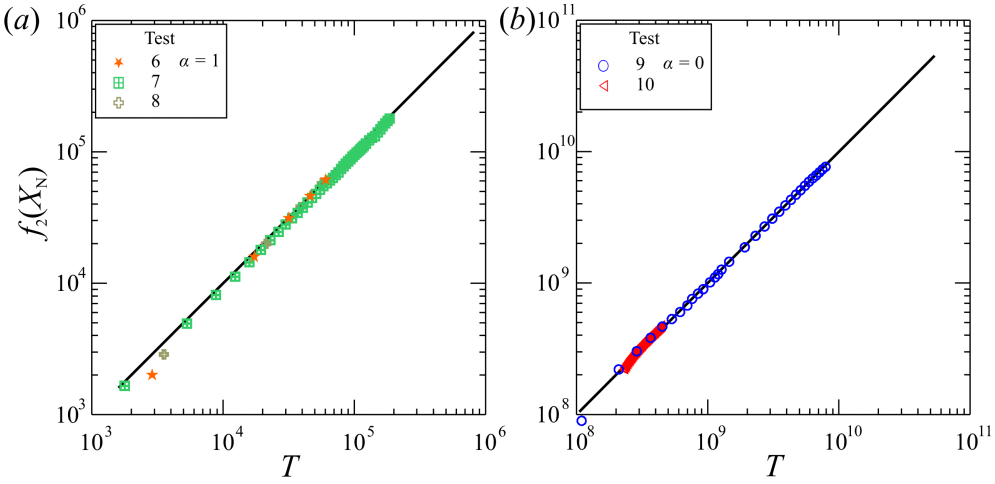

Fig. 7 Experimental results for horizontal right triangular channels in different sets of tests. The variables X_N and T are nondimensional and are scaled according to Eq. (48), with $f_2(X_N) = [(X_N/\eta_N)(2m/K_t)^{n/(n+1)}]^{1/F_{1t}}$. The solid line represents the theoretical prediction.

waves is strongly affected by the shape of the channel, we expect the peak fluid velocity also to be larger than the uniform current speed in semicircular and triangular channels; this velocity field pushes the current front end, which in turn moves faster than the uniform speed. In some of the present tests, the front of the current advanced with an average speed greater than the normal speed, but still lower than that predicted by the present model; this finding is qualitatively consistent with the mechanism of current advancement described above. While the model adopted herein does

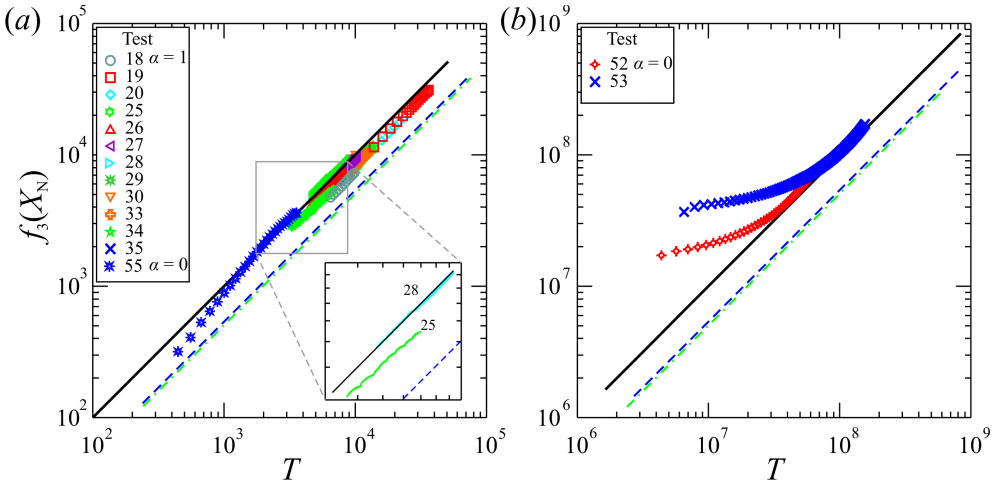

Fig. 8 Experimental results for inclined semicircular channels in different sets of tests. The variables X_N and T are nondimensional and are scaled according to Eq. (32), with $f_3(X_N) = [(X_N^{5n+2}/g_c^{3n})[16(n+1)/(3\sqrt{2}(5n+2))]^{2(n+1)}]^{1/[2\alpha(n+1)+3n]}$. The solid line represents the theoretical prediction; the blue dashed and green dash-dotted lines represent the normal speeds for a uniform current of shear-thinning ($n = 0.42$) and Newtonian liquids, respectively. The inset in Figure 8a shows an enlargement of a portion of the figure, illustrating the behaviour of currents with roll waves (tests 25 and 28).

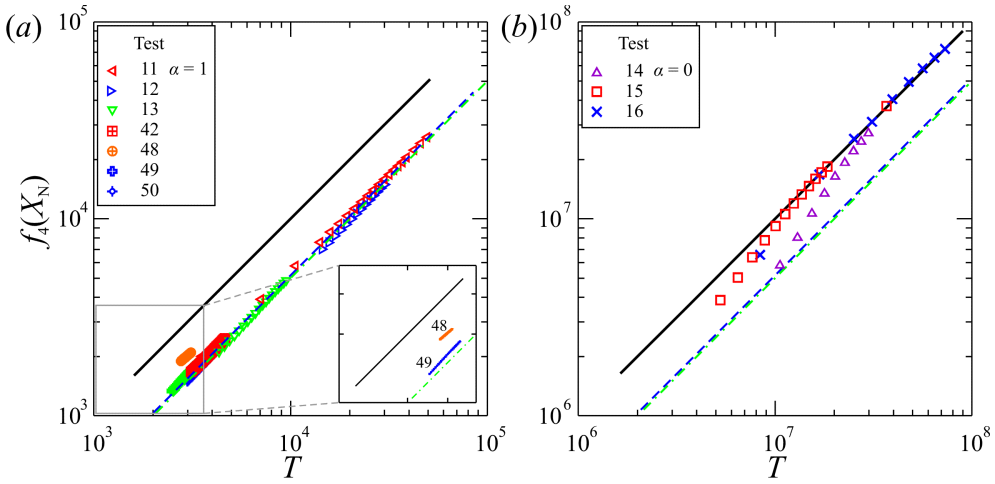

Fig. 9 Experimental results for inclined right triangular channels in different sets of tests. The variables X_N and T are nondimensional and are scaled according to Eq. (58), with $f_4(X_N) = [(X_N^{3n+1}/g_t^{2n})[(n+1)/(3n+1)]^{(n+1)}]^{1/[\alpha(n+1)+2n]}$. The solid line represents the theoretical prediction; the blue dashed and green dash-dotted lines represent the normal speeds for a uniform current of shear-thinning ($n = 0.42$) and Newtonian liquids, respectively. The inset in Figure 9a shows an enlargement of a portion of the figure, illustrating the behaviour of currents in a metastable state (tests 48 and 49).

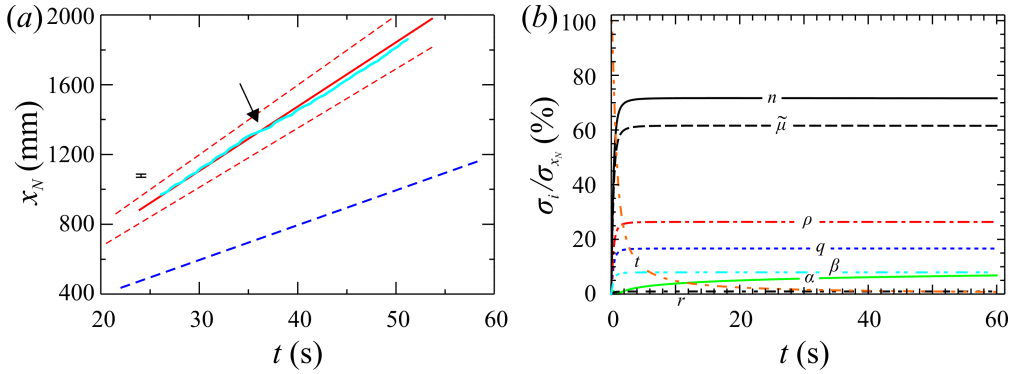

Fig. 10 Left panel: position of the current front for test 28 (semicircular inclined channel, $n = 0.42 \pm 2.5\%$, $\tilde{\mu} = 0.67 \pm 3.5\%$ Pa s^n, $\rho = 1175 \pm 1.0\%$ kg m^{-3}, $q = 0.30 \pm 1\%$ ml s^{-1}, $\beta = 30.6^\circ \pm 0.5\%$, $\alpha = 1.0 \pm 0.1\%$, and $r = 74.5 \pm 1\%$ mm, uncertainty expressed as one standard deviation). The thick red and thin light blue solid lines are the theoretical prediction and the experimental results, respectively; the dashed red lines are the 95% confidence limits and the thick blue dashed line represents the uniform motion (normal speed). The arrow indicates the transition to a different flow regime. The error bar equal to ± 2 times the experimental uncertainty in detecting the front end position of the current is indicated for comparison. Right panel: sensitivity analysis for the length of the gravity current in an inclined channel with a semicircular cross-section. The ratio of the standard deviation, σ_i, of the ith parameter and the total standard deviation, σ_{x_N}, is shown assuming an uncertainty of 1% for each parameter. The uncertainty in time is assumed to be equal to 1/50 s, i.e., half the time interval between two subsequent frames.

not consider inertia, the appearance of incipient roll waves and/or metastable configurations suggests that inertial effects or other secondary effects were not entirely negligible. Upon examining the position of the current front against time in greater detail in specific tests exhibiting roll waves (e.g., test 28 conducted in a semicircular inclined channel, Figure 10a), it is seen that the current propagation is initially correctly predicted by the present model. Then, the speed of the front end decreases quite abruptly as soon as the roll waves increase in length. This was also documented for other tests showing longer roll waves, and confidence intervals of the same order as those shown in Figure 10a were obtained. On the basis of these findings, it can be concluded that the present model correctly interprets the advancement of the current before the transition between incipient roll waves and roll waves. As soon as the roll waves increase in length, part of the energy is dissipated in the breaking process of the bores, and the front of the current reduces its speed. To capture this transition in triangular channels, numerous tests were added to the initially planned sequence. The channel material was also changed from aluminium to PVC to detect the possible effects of the contact angle and/or any electrical effects evident in microchannel viscous flows (see, e.g., Yang and Li [27]); however no significant change was observed in the propagation rate. Notably, tests conducted in identical conditions yielded different values for the speed of the front end of the current; this indicated the metastability of the flow, which is highly sensitive to minimal disturbances.

An uncertainty analysis was conducted by expressing the length of the current, x_N, as a function of the problem parameters and time, and by expanding x_N in a Taylor series to first order. After calculating the contribution of each parameter, the total un-

certainty in x_N was obtained by summing the individual contributions in quadrature as

$$\sigma_{x_N} = \sqrt{\left(\frac{\partial x_N}{\partial n}\right)^2 \sigma_n^2 + \left(\frac{\partial x_N}{\partial \widetilde{\mu}}\right)^2 \sigma_{\widetilde{\mu}}^2 + \ldots}, \tag{69}$$

where the symbols σ_i denote the standard deviation, which is assumed to be an estimate of the uncertainty. Figure 10b depicts the sensitivity of the model to the uncertainty in the parameters as the ratio between the standard deviation associated with each parameter and the total standard deviation, assuming a fixed uncertainty of 1% for each parameter. The highest ratio is associated with the rheological parameters n and $\widetilde{\mu}$, accounting for more than 80% of the total standard deviation of x_N. This is because in the present tests, the uncertainties in n and $\widetilde{\mu}$ are by far the most relevant - all the other sources of uncertainty are almost trivial.

5 Conclusions

We investigated the flow of laminar gravity currents of power-law liquids in horizontal and inclined channels having different cross-sectional shapes, namely semicircular and right triangular, theoretically and experimentally. The theoretical solutions are self-similar or based on the method of characteristics, and allow the evaluation of the position of the current front and the thickness of its profile, extending the Newtonian results of Takagy and Huppert [20, 21]. Laboratory experiments were conducted with liquids of different rheologies in semicircular and triangular channels. The main conclusions of our work are:

- The position of the current front depends on (i) the volume parameter α, (ii) the liquid rheology, and (iii) the channel inclination and shape of the cross-section. The latter factor influences the mass balance equation and modulates the downstream evolution of the current. Critical values of α are determined for horizontal channels as a function of behaviour index n as $\alpha_c = n/(n+1)$, and for inclined channels as $\alpha_c = 1$, irrespective of cross-section geometry. For triangular cross-sections, a maximum (minimum) value of the rate of spreading is attained for $\alpha < \alpha_c$ ($\alpha > \alpha_c$).
- The position of the current front obtained experimentally is generally in good agreement with theory. For tests in inclined channels with $\alpha = 1$, a variety of flow regimes typical of open-channel flows were observed at the end of the tests: uniform flow with normal depth, incipient roll waves, roll waves, metastable conditions. The final propagation rate of the current front was overpredicted by the model, while the presence of roll waves suggested the influence of inertia or other secondary effects. Upon examining the rate of propagation of the current over time, it was discovered that the theoretical solution accurately describes the phenomenon before the transition between incipient roll waves and roll waves. As these require a sufficient channel length to develop, the final fate of the currents analysed in the present tests is not known. However, on the basis of our experimental results, we infer that the profile predicted for inclined channels in the

present model is a limiting profile of the current and marks the transition to a different flow regime.
- The rheology of complex liquids is usually of concern in laminar flow models because it is often not adequately known or described. This is confirmed by the present study, where the rheological parameters are shown to be the main source of uncertainty. This behaviour supports the use of carefully designed laboratory experiments as rheometric tests.
- The results obtained may prove useful in analysing the joint influence of rheology, channel shape, and volume growth rate in environmental flows, such as turbidity currents, avalanches, and pyroclastic flows of non-Newtonian fluids characterised by negligible yield stress.

Acknowledgements Support from Università di Bologna RFO (Ricerca Fondamentale Orientata) 2011 and 2012 is gratefully acknowledged.

References

1. J. E. Simpson. Gravity currents in the laboratory, atmosphere, and ocean. *Ann. Rev. Fl. Mech.*, 14:213–234, 1982.
2. H. E. Huppert. The intrusion of fluid mechanics into geology. *J. Fluid Mech.*, 173:557–598, 1986.
3. M. Ungarish. *An Introduction to Gravity Currents and Intrusions*. CRC Press, 2010.
4. H. E. Huppert. The propagation of two-dimensional and axisymmetric viscous gravity currents over a rigid horizontal surface. *J. Fluid Mech.*, 121:43–58, 1982.
5. N. Didden and T. Maxworthy. The viscous spreading of plane and axisymmetric gravity currents. *J. Fluid Mech.*, 121:27–42, 1982.
6. H. Pinkerton and R. S. J. Sparks. Field measurements of the rheology of lava. *Nature*, 276:383–385, 1978.
7. D. Takagi and H. E. Huppert. Initial advance of long lava flows in open channels. *J. Volcanol. Geotherm. Res.*, 195:121–126, 2010.
8. R. Ugarelli and V. Di Federico. Transition from supercritical to subcritical regime in free surface flow of yield stress fluids. *Geophys. Res. Lett.*, 34:L21402, 2007.
9. I. Sonder, B. Zimanowski, and R. Buttner. Non-Newtonian viscosity of basaltic magma. *Geophysical Research Letters*, 33:L02303, 2006.
10. C.-O. Ng and C. G. Mei. Roll waves on a shallow layer of mud modelled as a power-law fluid. *J. Fluid Mech.*, 263:151–183, 2004.
11. J. Burger, R. Haldenwang, and N. Alderman. Friction factor - Reynolds number relationship for laminar flow of non-Newtonian fluids in open channels of different cross-sectional shapes. *Chem. Eng. Sci.*, 85:3549–3556, 2010.
12. J.P. Pascal. Gravity flow of a non-Newtonian fluid sheet on an inclined plane. *Int. J. Eng. Sci.*, 29(10):1307–1313, 1991.
13. J. Gratton, F. Minotti, and S.M. Mahajan. Theory of creeping gravity currents of a non-Newtonian liquid. *Phys. Rev. E*, 60(6):6960–6967, 1999.

14. V. Di Federico, S. Malavasi, and S. Cintoli. Viscous spreading of non-Newtonian gravity currents on a plane. *Meccanica*, 41:207–217, 2006.
15. M.R. Chowdhury and F.Y. Testik. Viscous propagation of two-dimensional non-Newtonian gravity currents. *Fluid Dyn. Res.*, 44:045502, 2012.
16. R. Sayag and M. G. Worster. Axisymmetric gravity currents of power-law fluids over a rigid horizontal surface. *J. Fluid Mech.*, 716:R5–1–11, 2013.
17. S. Longo, V. Di Federico, R. Archetti, L. Chiapponi, V. Ciriello, and M. Ungarish. On the axisymmetric spreading of non-Newtonian power-law gravity currents of time-dependent volume: An experimental and theoretical investigation focused on the inference of rheological parameters. *J. Non-Newton. Fluid Mech.*, 201:69–79, 2013.
18. M.P. Piau and K. Debiane. Consistometers rheometry of power-law viscous fluids. *J. Non-Newton. Fluid Mech*, 127:213–224, 2005.
19. M. R. Jacobson and F. Y. Testik. Turbulent entrainment into fluid mud gravity currents. *Environ. Fluid Mech.*, DOI 10.1007/s10652-014-9344-5, 2014.
20. D. Takagi and H. E. Huppert. The effect of confining boundaries on viscous gravity currents. *J. Fluid Mech.*, 577:495–505, 2007.
21. D. Takagi and H. E. Huppert. Viscous gravity currents inside confining channels and fractures. *Phys. Fluids*, 20:023104, 2008.
22. C.C. Mei and M. Yuhi. Slow flow of a Bingham fluid in a shallow channel of finite width. *J. Fluid Mech.*, 431:135–159, 2001.
23. H. E. Huppert. Flow and instability of a viscous current down a slope. *Nature*, 300:427–429, 1982.
24. Y. S. Muzychka and J. Edge. Laminar non-Newtonian fluid flow in noncircular ducts and microchannels. *J. Fluid Eng.-T ASME*, 130:111201–7, 2008.
25. P. Y. Julien and D. M. Hartley. Formation of roll waves in laminar sheet flow. *J. Hydraul. Res.*, 24:1–17, 1986.
26. S. Longo. Roll waves on a shallow layer of a dilatant fluid. *Eur. J. Mech. B-Fluids*, 30:57–67, 2011.
27. C. Yang and D. Li. Analysis of electrokinetic effects on the liquid flow in rectangular microchannels. *Colloid Surface A*, 143:339–353, 1998.

Shape	Reference	Horizontal ($\beta = 0$)	Reference	Inclined ($\beta > 0$)
Narrow ($k = 1/2$)	tp	$\frac{3(n+\alpha)+2n\alpha}{5n+6}$	tp	$\frac{2\alpha(n+1)+3n}{5n+2}$
V-shaped ($k = 1$)	tp	$\frac{\alpha(n+2)+2n}{3n+4}$	tp	$\frac{\alpha(n+1)+2n}{3n+1}$
Semicircular ($k = 2$)	tp	$\frac{2\alpha(n+2)+3n}{5n+7}$	tp	$\frac{2\alpha(n+1)+3n}{5n+2}$
Rectangular ($k \to \infty$)	GM	$\frac{\alpha(n+2)+n}{2n+3}$	tp	$\frac{\alpha(n+1)+n}{2n+1}$

Table 1 Current propagation rates in horizontal and inclined channels of different shapes. "GM" and "tp" refer to Gratton et al. [13] and this paper, respectively. For $n = 1$, these results are consistent with the data listed in Table I of Takagi and Huppert [21].

Test	shape	β	α	q	n	$\widetilde{\mu}$	ρ	Re	Fr	state
		(deg)		(ml $s^{-\alpha}$)		(Pa s^n)	(kg m^{-3})			
21	c(2)	0.0	0.0	143.6	0.42	0.67	1175			
24	c(2)	0.0	0.0	311.2	0.42	0.67	1175			
52	c(2)	7.4	0.0	126	0.42	0.67	1175			
53	c(2)	4.5	0.0	130	0.42	0.67	1175			
55	c(2)	4.5	0.0	192	1.57	0.40	1200			
1	c(1)	0.0	1.0	1.35	0.42	0.67	1175			
2	c(1)	0.0	1.0	4.08	0.42	0.67	1175			
3	c(1)	0.0	1.0	0.57	0.42	0.67	1175			
5	c(1)	0.0	1.0	2.17	1.00	0.16	1241			
18	c(2)	4.0	1.0	0.79	1.00	0.16	1241	6.4	0.11	me
19	c(2)	4.0	1.0	0.78	0.42	0.67	1175	1.2	0.10	me
20	c(2)	5.5	1.0	2.34	0.42	0.67	1175	6.0	0.27	me
25	c(2)	30.6	1.0	3.94	0.42	0.67	1175	62.5	1.98	rw
26	c(2)	30.6	1.0	0.77	0.42	0.67	1175	9.8	0.76	rw
27	c(2)	30.6	1.0	0.21	0.42	0.67	1175	2.2	0.35	
28	c(2)	30.6	1.0	0.30	0.42	0.67	1175	3.3	0.43	rw
29	c(2)	30.6	1.0	0.24	0.42	0.67	1175	2.6	0.37	irw
30	c(2)	30.6	1.0	0.18	0.42	0.67	1175	1.9	0.32	
33	c(2)	18.0	1.0	0.94	0.42	0.67	1175	7.2	0.50	rw
34	c(2)	18.0	1.0	0.54	0.42	0.67	1175	3.9	0.36	
35	c(2)	18.0	1.0	1.64	0.42	0.67	1175	13.6	0.69	rw
9	t	0.0	0.0	286	0.42	0.67	1175			
10	t	0.0	0.0	430	0.42	0.67	1175			
14	t	5.5	0.0	163.9	0.42	0.67	1175			
15	t	8.8	0.0	68.0	0.42	0.67	1175			
16	t	5.5	0.0	104.1	0.42	0.67	1175			
6	t	0.0	1.0	2.14	0.42	0.67	1175			
7	t	0.0	1.0	0.54	0.42	0.67	1175			
8	t	0.0	1.0	4.33	0.42	0.67	1175			
11	t	5.5	1.0	4.14	0.42	0.67	1175	10.5	0.54	u
12	t	8.6	1.0	1.86	0.42	0.67	1175	7.6	0.57	u
13	t	5.5	1.0	0.81	0.42	0.67	1175	1.8	0.22	u
42	t	18.1	1.0	3.82	0.42	0.67	1175	40	1.93	
48	t	30.5	1.0	2.29	1.00	0.16	1241	3.3	0.78	me
49	t	30.5	1.0	3.62	1.00	0.16	1241	4.6	0.92	me
50	t	30.5	1.0	2.31	1.00	0.16	1241	3.3	0.78	u

Table 2 Experimental parameters for all tests. The symbols c(1) and c(2) indicate a semicircular section with $r = 119$ mm and $r = 74.5$ mm, respectively, whereas t indicates a triangular section with $2\theta = 90^\circ$. Values of global Reynolds and Froude numbers are listed when $\alpha = 1$ and $\beta > 0$. In the last column, "me" indicates a metastable state, "rw" indicates the presence of roll waves, "irw" indicates incipient roll waves, and "u" indicates uniform flow with normal velocity.